The Astrophysical Journal, 898:154 (13pp), 2020 August 1 https://doi.org/10.3847/1538-4357/ab9ab6

Observations of Particle Acceleration in Magnetic Reconnection–driven Turbulence

R. E. Ergun[1,2], N. Ahmadi[2], L. Kromyda[1,2], S. J. Schwartz[2], A. Chasapis[2], S. Hoilijoki[2], F. D. Wilder[2], J. E. Stawarz[3], K. A. Goodrich[4], D. L. Turner[5], I. J. Cohen[5], S. T. Bingham[5], J. C. Holmes[6], R. Nakamura[6], F. Pucci[2], R. B. Torbert[7,8], J. L. Burch[8], P.-A. Lindqvist[9], R. J. Strangeway[10], O. Le Contel[11], and B. L. Giles[12]
[1] Department of Astrophysical and Planetary Sciences, University of Colorado, Boulder, CO, USA
[2] Laboratory for Atmospheric and Space Physics, University of Colorado, Boulder, CO, USA
[3] The Blackett Laboratory, Imperial College London, UK
[4] Space Sciences Laboratory, University of California, Berkeley, CA, USA
[5] Johns Hopkins University Applied Physics Laboratory, Laurel, MD, USA
[6] Space Research Institute, Austrian Academy of Sciences, Graz, Austria
[7] University of New Hampshire, Durham, NH, USA
[8] Southwest Research Institute, San Antonio, TX, USA
[9] KTH Royal Institute of Technology, Stockholm, Sweden
[10] University of California, Los Angeles, Los Angeles, CA, USA
[11] Laboratoire de Physique des Plasmas, CNRS/IP Paris/Sorbonne Université/Université Paris-Saclay/Observatoire de Paris, Paris, France
[12] NASA, Goddard Space Flight Center, Greenbelt, MD, USA
Received 2020 February 6; revised 2020 May 21; accepted 2020 May 21; published 2020 August 4

Abstract

The Magnetospheric Multiscale Mission observes, in detail, charged particle heating and substantial nonthermal acceleration in a region of strong turbulence ($|\delta \boldsymbol{B}|/|\boldsymbol{B}| \sim 1$, where $\boldsymbol{B}$ is the magnetic field) that surrounds a magnetic reconnection *X*-line. Magnetic reconnection enables magnetic field annihilation in a volume that far exceeds that of the diffusion region. The formidable magnetic field annihilation breaks into strong, intermittent turbulence with magnetic field energy as the driver. The strong, intermittent turbulence appears to generate the necessary conditions for nonthermal acceleration. It creates intense, localized currents ($\boldsymbol{J}$) and unusually large-amplitude electric fields ($\boldsymbol{E}$). The combination of turbulence-generated $\boldsymbol{E}$ and $\boldsymbol{J}$ results in a significant net positive mean of $\boldsymbol{J} \cdot \boldsymbol{E}$, which signifies particle energization. Ion and electron heating rates are such that they experience a fourfold increase from their initial temperature. Importantly, the strong turbulence also generates magnetic holes or depletions in $|\boldsymbol{B}|$ that can trap particles. Trapping considerably increases the dwell time of a subset of particles in the turbulent region, which results in significant nonthermal particle acceleration. The direct observation of strong turbulence that is enabled by magnetic reconnection with nonthermal particle acceleration has far-reaching implications, since turbulence in plasmas is pervasive and may occupy significant volumes of the interstellar medium and intergalactic space. For example, strong turbulence from magnetic field annihilation in the supernova nebulae may dominate large volumes. As such, this observed energization process could plausibly contribute to the supply and development of the cosmic-ray spectrum.

Unified Astronomy Thesaurus concepts: Space plasmas (1544); Plasma astrophysics (1261); Plasma physics (2089)

1. Introduction

Magnetic reconnection is a key electromagnetic process that has been observed or postulated to occur in many distinct plasmas. In the heliosphere, magnetic reconnection is essential to the development of solar flares (e.g., Parker 1957; Priest & Forbes 2002), the evolution of solar and stellar winds (Gosling et al. 2005; Gosling 2007), and the energy imparted into Earth's and planetary magnetospheres (Dungey 1961; Paschmann et al. 1979). Magnetic reconnection is seen in laboratory plasmas in circumstances such as sawtooth crashes (von Goeler et al. 1974) and has been the focus of several laboratory experiments (see Yamada et al. 2010). After the pioneering observations and simulations (e.g., Paschmann et al. 1979; Hesse et al. 1999; Birn et al. 2001; Øieroset et al. 2001; Drake et al. 2003; also see Yamada et al. 2010 and references within), magnetic reconnection has been established as a widespread physical process that may be active in pulsar nebulae (e.g., Uzdensky et al. 2011), central to energy conversion in gamma-ray bursts (Thompson 1994; Spruit et al. 2001; Lyutikov et al. 2003), and the source of soft gamma-ray repeaters from neutron stars (e.g., Uzdensky et al. 2011); result in AGN nonthermal emission (Kumar & Zhang 2015); and influence electromagnetic emissions near black holes (Koide et al. 2006). It has also been postulated to be active in the interstellar medium (Zweibel 1989).

While magnetic reconnection may be a central process for magnetic field annihilation in space plasmas, it is important to understand that the magnetic field energy annihilation enabled by magnetic reconnection over a large volume can exceed that inside of the diffusion regions by many orders of magnitude (e.g., Bandyopadhyay et al. 2018). Furthermore, the region of strong turbulence surrounding magnetic reconnection is observed to have depleted plasma density (e.g., Ergun et al. 2018), which results in unusually large magnetic energy transfer per particle and thus very strong heating and/or acceleration. Such depleted regions may break into strong turbulence ($|\delta \boldsymbol{B}|/|\boldsymbol{B}| \sim 1$, where $\boldsymbol{B}$ is the magnetic field).

In this paper and a companion paper (Ergun et al. 2020), we investigate charged particle heating and acceleration to further the research on turbulence and particle acceleration. We present Magnetospheric Multiscale Mission (MMS; Burch et al. 2016) observations that demonstrate local charged particle heating and nonthermal acceleration in an extended region of strong turbulence surrounding a magnetic reconnection *X*-line. A critical ingredient for the observed heating appears to be the strong, localized currents ($\boldsymbol{J}$) and large-amplitude electric fields

($\boldsymbol{E}$) that are generated by strong, intermittent turbulence and result in a net positive average, $\langle \boldsymbol{J} \cdot \boldsymbol{E} \rangle$. Another critical ingredient for nonthermal acceleration is trapping by magnetic holes (e.g., Goodrich et al. 2016) or depletions in $|\boldsymbol{B}|$. Trapping apportions unequal dwell times of particles in heating regions, which develops a nonthermal tail in particle distributions. In addition, we show that as particles are heated, their speed and gyroradii increase, which, in the turbulent $\boldsymbol{E}$, promotes increased heating of higher-energy particles and thus amplifies the nonthermal tail.

This paper begins with an observational overview of magnetic reconnection and turbulence reported in an earlier letter (Ergun et al. 2018). Magnetic reconnection in the Earth's magnetotail is well established (Nagai et al. 1998; Øieroset et al. 2001; Paschmann 2008; Torbert et al. 2018), and electron acceleration has been previously observed (Øieroset et al. 2002; Imada et al. 2007; Retinó et al. 2008; Vaivads et al. 2011). Reconnection jets in the Earth's magnetotail known as bursty bulk flows (Baumjohann et al. 1989; Angelopoulos et al. 1992, 1994) also are associated with turbulence, heating, and acceleration (Borovsky et al. 1997; Vörös et al. 2004; Weygand et al. 2005; Ergun et al. 2015). Recent simulations have linked magnetic reconnection, turbulence, and particle acceleration (e.g., Lu et al. 2019) in the Earth's magnetotail.

We follow the overview with a discussion of the observed properties of the strong turbulence that envelops the magnetic reconnection region, demonstrating intermittency. We investigate specific properties of the $\boldsymbol{E}$ turbulence, including establishing correlation lengths and timescales. Next, we show several examples of local electron acceleration. A key point is that the core thermal electrons often show higher parallel temperatures, whereas the nonthermal accelerated electrons have higher perpendicular energy and appear to be trapped in a depleted magnetic field. Ion distributions show heating and have an accelerated tail. A companion paper (Ergun et al. 2020) uses test-particle simulations to better understand the electron and ion energization in strong turbulence.

2. Observations

2.1. Overview of the Observations

The observations in this paper are from the MMS satellites (Burch et al. 2016), which are designed to study magnetic reconnection at electron scales. The MMS employs four spacecraft that are in a tetrahedral configuration. Figure 1 displays 1 hr of data from MMS2 taken in the Earth's magnetotail ~23 Earth radii (R_E) from Earth. The location of the satellites and the relative positions are in Figures 1(i) and (j). During this 1 hr period, there are two intervals of strong turbulence that are marked on the top of the plot. Figure 1(a) plots the omnidirectional ion flux in the energy range from ~60 to ~600 keV as a function of time. These spectrograms combine measurements from all four MMS spacecraft made by a non-mass-discriminating energetic ion spectrometer (Blake et al. 2016). These detectors are part of the Energetic Particle Detector (EPD) investigation on MMS (Mauk et al. 2016). The spacecraft separations are considerably smaller than the ion gyroradii (ρ_i), so combining the data improves counting statistics and angular coverage. Figure 1(b) plots the ion differential energy flux in the energy range of ~10 eV to ~25 keV that is measured by the Fast Plasma Instrument (FPI; Pollock et al. 2016). These data and all other data in Figure 1 are from the MMS2 spacecraft. Outside of the turbulent regions, for example, 07:38–07:54 UT in Figure 1(b), the thermal ion population temperature (T_i) ranges from ~4 to ~6 keV. During the intervals marked as turbulent regions, T_i is noticeably higher. At times, a substantial part of the ion energy flux exceeds the maximum energy (25 keV) of the FPI instrument (Figure 2(b)), making T_i difficult to determine accurately. At the same time, high-energy ion fluxes exceeding 100 keV (Figure 1(a)) increase well above that expected from a Maxwellian distribution, which indicates nonthermal ion acceleration.

Figure 1(c) plots the electron particle flux in the energy range of ~50 to ~500 keV (Blake et al. 2016; Mauk et al. 2016), and Figure 1(d) plots the electron differential energy flux in the energy range of ~10 eV to ~25 keV (Pollock et al. 2016). The electron temperatures (T_e) are roughly 1/4 to 1/5 of the ion temperatures and show a similar pattern; T_e is relatively steady at ~1 keV outside of the turbulent regions and noticeably rises to between 5 and 10 keV inside of the turbulent regions. High-energy electron fluxes exceeding 100 keV (Figure 1(c)) increase considerably, indicating nonthermal electron acceleration.

Figure 1(e) displays three components of the magnetic field ($\boldsymbol{B}$), with $|\boldsymbol{B}|$ plotted in black. Figures 1(f) and (g) plot the electric field ($\boldsymbol{E}$) and ion bulk velocity (V_{ion}). Here $\boldsymbol{B}$, $\boldsymbol{E}$, and $\boldsymbol{V}_{ion}$ are in the geocentric solar ecliptic (GSE) coordinate system; X is toward the Sun, Z is normal to the ecliptic, and Y completes the system. The ion velocity has an increased uncertainty in regions where T_i exceeds the energy range of the FPI analyzer. The $\boldsymbol{B}$ and $\boldsymbol{E}$ measurements are described in several papers (Ergun et al. 2016; Le Contel et al. 2016; Lindqvist et al. 2016; Russell et al. 2016; Torbert et al. 2016).

Clearly visible fluctuations in $\boldsymbol{B}$ and $\boldsymbol{E}$ (Figures 1(e) and (f)) are concurrent with bulk heating of the thermal ion and electron populations (Figures 1(b) and (d)) and enhanced, nonthermal fluxes of energetic ions and electrons (Figures 1(a) and (c)). In turbulent region 1, the X-component of $\boldsymbol{V}_{ion}$ (blue line in Figure 1(g)) reverses from negative (anti-earthward) to positive (earthward) during the turbulent event at ~07:28:30 UT. At roughly the same time, $\langle B_z \rangle$ (red line in Figure 1(e)) reverses in the same fashion (difficult to see by eye). The combination of a V_x reversal and a B_z reversal (negative to positive) is a well-established indicator of magnetic reconnection in the Earth's magnetotail (Nagai et al. 1998; Øieroset et al. 2001; Torbert et al. 2018).

Figure 1(i) shows an interpretation of the observations in turbulent region 1, which is one of a series of magnetic reconnection events on 2017 July 26 (not shown). The events are spaced at 30–40 minute intervals. The magnetotail is in a relatively low-activity state at ~07:20 UT. Just before ~07:22 UT (Figure 1(i), top diagram), a magnetic reconnection event begins earthward of the MMS satellites. Shortly after, an anti-earthward ion jet ($V_x < -500$ km s^{-1}) is detected by MMS. At the same time, $\langle B_z \rangle$ becomes negative, and strong fluctuations in ion fluxes, electron fluxes, $\boldsymbol{B}$, and $\boldsymbol{E}$ initiate.

Magnetic reconnection regions in the Earth's magnetotail have been observed to propagate at speeds of the order of 100–200 km s^{-1} anti-earthward (e.g., Nagai et al. 1998; Øieroset et al. 2001; Torbert et al. 2018). At ~07:28 UT, both V_x and B_z reverse sign to positive within ~30 s of each other, indicating that the magnetic reconnection region passes by the MMS satellites (Figure 1(i), middle diagram). Neither the ion diffusion region nor the electron diffusion region can be

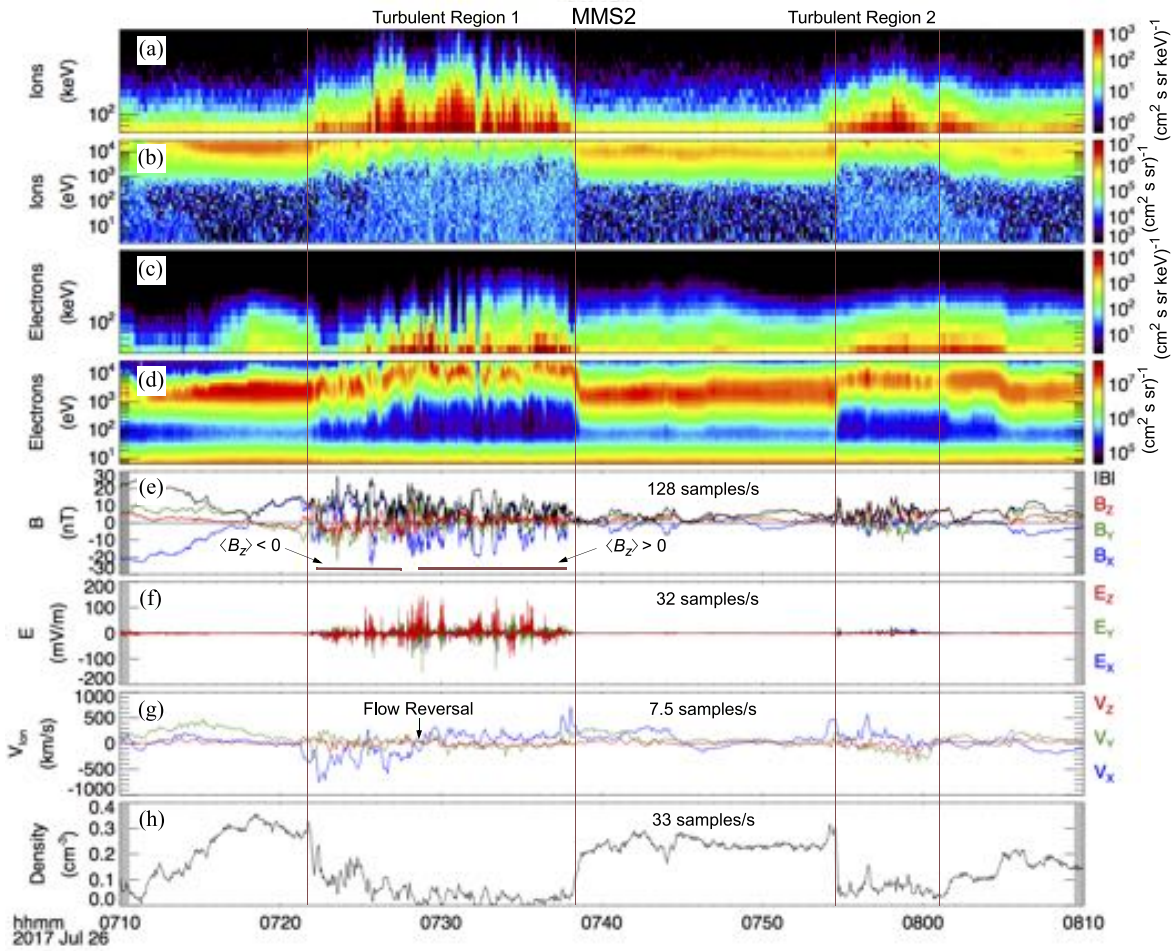

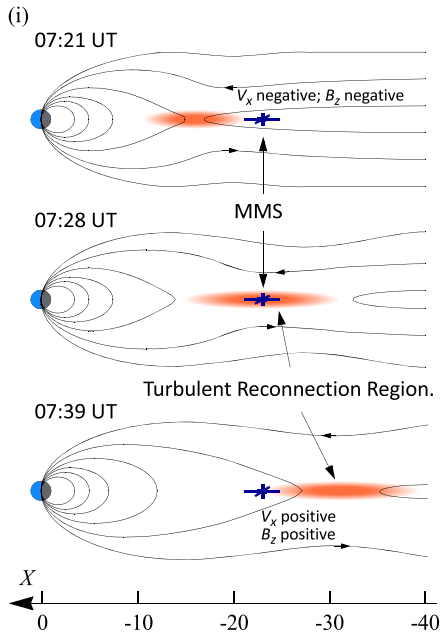

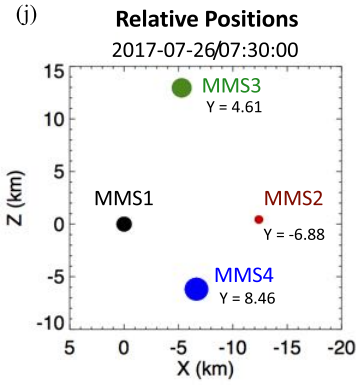

MMS1 at [-23.0, 7.7, 5.0] R_E in GSE coordinates.

Separations:
MMS1-2: 14.18 km
MMS1-3: 14.73 km
MMS1-4: 12.41 km
MMS2-3: 18.41 km
MMS2-4: 17.66 km
MMS3-4: 19.57 km

Mean Plasma Conditions[1]

Parameter	Value
$\langle n_e \rangle$	0.03 cm^{-3}
$\langle T_e \rangle$	4 keV
$\langle T_i \rangle$[Note 2]	20 keV
$\langle \lvert \boldsymbol{B} \rvert \rangle$	10 nT
$\langle E_y \rangle$	2.5 mV m^{-1}
$\langle f_{pe} \rangle$	1.6 kHz
$\langle f_{ce} \rangle$	280 Hz
$\langle f_{pi} \rangle$	37 Hz
$\langle f_{ci} \rangle$	0.15 Hz
$\langle v_{the} \rangle$	26500 km s^{-1}
$\langle v_{thi} \rangle$[Note 2]	1400 km s^{-1}
$\langle V_A \rangle$	1400 km s^{-1}
$\langle V_S \rangle$[Note 2]	1800 km s^{-1}
$\langle V_F \rangle$[Note 2]	2250 km s^{-1}
$\langle \rho_e \rangle$	15 km
$\langle \rho_i \rangle$[Note 2]	1450 km
$\langle d_e \rangle$	30 km
$\langle d_i \rangle$	1290 km
$\langle \lambda_{de} \rangle$	3 km

[1]07:22 to 07:38 UT.
[2]Estimate. Ion temperature not directly measured.

Figure 1. Strong turbulence in the Earth's magnetotail. (a) Omnidirectional ion flux (intensity) as a function of energy (vertical axis) and time (horizontal axis). The energy range is from 60 to 600 keV. Data from all four MMS spacecraft are combined to form this plot. (b) Omnidirectional ion differential energy flux as a function of energy and time. The energy range is from 10 eV to 25 keV. (c) Omnidirectional electron flux as a function of energy and time. The energy range is from 50 to 500 keV. (d) Omnidirectional electron differential energy flux as a function of energy and time. The energy range is from 10 eV to 25 keV. (e) $\boldsymbol{B}$ in GSE coordinates. The color code is to the right of the box. (f) $\boldsymbol{E}$ in GSE coordinates. (g) $V_{\rm ion}$ in GSE coordinates. (h) Electron density. (i) Interpretation of turbulent region 1. Magnetic reconnection (and the accompanying turbulent region) is observed to retreat tailward at 100–200 km s^{-1} (Ergun et al. 2018). (j) Relative positions of the MMS satellite, position of MMS1, and separation distances. At the bottom right is a table of the average values of the plasma parameters.

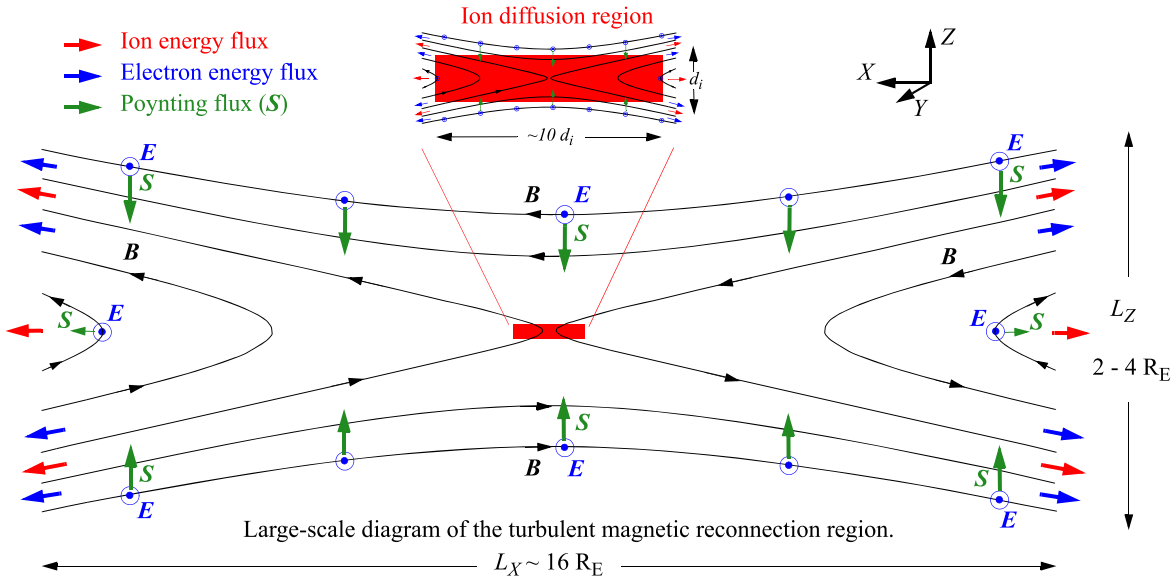

Figure 2. Diagram of turbulent region 1. The turbulent region occupies a far larger volume than the diffusion region of magnetic reconnection. Magnetic reconnection enables an out-of-plane electric field (E_y) of ~2.8 mV m^{-1} to develop. Here $|\boldsymbol{B}|$ in the lobe regions is ~20 nT, which results in Poynting flux of ~45 μW m^{-2} entering along the extent of the region (L_x) from both lobes. The energy is transported out of the region by electrons and ions passing through.

unequivocally detected, as the entire region is embedded in strong turbulence. The diffusion regions also may have passed to the north ($+Z$) or south ($-Z$) of the MMS tetrahedron. After ~07:28 UT, the MMS satellites are in the earthward jet of magnetic reconnection. At ~07:38 UT, the turbulence ceases, as either the magnetic reconnection region propagates well away from the MMS satellites or the magnetic reconnection terminates (Figure 1(i), bottom diagram).

Turbulent region 1 is related to a magnetic reconnection event that is retreating away from Earth. Figure 2 diagrams the extended magnetic reconnection and turbulent region. Given a retreat velocity of ~100 km s^{-1} (Ergun et al. 2018), the turbulent region, which endures for ~17 minutes, extends roughly 16 R_E (10^8 m) in the X-direction, which is labeled in Figure 2. From the MMS observations, $\langle E_y \rangle$ in the turbulent region is ~2.8 $\pm$ 0.5 mV m^{-1} and B_x in the northern lobe is ~20 nT (−20 nT in the southern lobe). The average Poynting flux entering the turbulent region from each lobe is

$$\langle S_z \rangle = \frac{E \times B}{\mu_o} \approx 45\ \mu\text{W m}^{-2}. \quad (1)$$

This energy flux originates from magnetic energy that is stored in the lobes. In contrast, our simple cartoon indicates that comparatively little Poynting flux is leaving the turbulent magnetic reconnection region (through the right and left sides of the turbulent region in Figure 2), since $\langle B_z \rangle < \langle B_x \rangle$ and $L_z < L_x$. As a result, most of the Poynting flux energy must be absorbed by the particles of the plasma sheet. Assuming a plasma sheet thickness of 2–4 R_E and using the measured average plasma density $\langle n \rangle \approx 0.03$ cm^{-3}, each ion–electron pair is energized at a rate of 1.5–3.0 keV s^{-1} (energy enters from both lobes). Direct measurement of $\langle \boldsymbol{J} \cdot \boldsymbol{E} \rangle = 3.4 \pm 1$ keV s^{-1} per particle pair during this event supports this rate of electromagnetic energy transfer into particle energy (the calculation of $\langle \boldsymbol{J} \cdot \boldsymbol{E} \rangle$ is discussed in Section 2.3). As indicated in Figure 2, the primary energy loss from the turbulent region is via particle transport.

Another important aspect of the magnetotail region is that the lobes have low density (and low plasma β). Thus, the ratio of Poynting flux ($\boldsymbol{E} \times \boldsymbol{B}/\mu_o$) to particle flux ($n\,\boldsymbol{E} \times \boldsymbol{B}/B^2$) is quite high along the lobe boundaries (>250 keV s^{-1} per particle pair if $n_{\text{lobe}} \sim 0.01$ cm^{-3}), which supports our postulation that existing plasma in the plasma sheet must absorb this Poynting flux. Furthermore, plasma is rapidly transported out of the turbulent region through the right and left boundaries in Figure 2. Since $\langle B_z \rangle < \langle B_x \rangle$, plasma exiting the region ($\sim nL_z E_y/|B_z|$) may exceed that entering ($\sim nL_x E_y/|B_x|$), even though $L_z < L_x$. The resulting low density (observed) amplifies the amount of energy that plasma sheet particles must absorb.

There are several important inferences that one can draw from this simple model. The diffusion region of magnetic reconnection (~1 d_i by ~10 d_i) contains only a small fraction of the volume of the turbulent region (L_Z by L_X in Figure 2). The electromagnetic energy transfer to particles inside of the diffusion region, while scientifically interesting and important, represents only a small fraction of the total electromagnetic energy transfer (that along the extended lobe boundaries) to particle energy that is enabled by magnetic reconnection. While magnetic reconnection is common in the Earth's magnetotail, this particular example of magnetic reconnection associated with strong turbulence is less frequent. This turbulent magnetic reconnection event, which followed a previous magnetic reconnection event, also has an abnormally low plasma density in the plasma sheet. We hypothesize that the low plasma density, likely the result of prior magnetic reconnection activity and/or a particularly low-β inflow from the lobes, results in an unusually large energy transfer (~3 keV s^{-1} per particle pair), which the plasma is unable to absorb in a laminar fashion.

For completeness, we discuss turbulent region 2 briefly. The turbulence begins shortly after 07:54 UT; V_x (blue line in Figure 1(g)) rises sharply to ~500 km s^{-1}, which indicates earthward flow. The most likely scenario is that a separate magnetic reconnection begins farther away from Earth than the MMS satellites circa 07:54 UT. The MMS satellites observe the earthward jet, then are engulfed in the turbulence as

the turbulent region expands. The bottom diagram in Figure 1(i) best represents turbulent region 2. As the magnetic reconnection region retreats away from Earth, $\boldsymbol{B}$ and $\boldsymbol{E}$ turbulence cease at ~08:01 UT. Unlike turbulent region 1, the indications of turbulence do not abruptly end. Energetic ions are detected for ~2 minutes after $\boldsymbol{B}$ and $\boldsymbol{E}$ fluctuations abate. The heated and energetic electrons linger for an additional ~2 minutes.

2.2. Characteristics of the Observed Turbulence

The MMS satellites have accurate measurements of $\boldsymbol{B}$, $\boldsymbol{E}$, and $\boldsymbol{J}$ allowing for a detailed analysis of turbulent dissipation and particle acceleration. Characteristics of $\boldsymbol{B}$ in turbulent regions have been studied extensively. However, the observed turbulence (Figure 1) is somewhat exceptional in that it is driven by magnetic reconnection, highly confined, and exceptionally strong; that is, $|\delta\boldsymbol{B}|/|\boldsymbol{B}|$ is near unity. Furthermore, comparatively little attention has been given to the characteristics of $\boldsymbol{E}$ in turbulent regions. In this section, we detail $\boldsymbol{E}$ and $\boldsymbol{B}$ in strong turbulence. We do not detail $\boldsymbol{V}$. While the FPI has significantly higher accuracy than that of previous space plasma missions, much of the ion population is outside of the measurement range, and low densities limit the accuracy in this particular event.

Studies of turbulence often begin with examining the power spectral density (PSD) of $\boldsymbol{B}$, such as was done in an earlier study (Ergun et al. 2018). The PSD of $\boldsymbol{B}$ as a function of wavenumber ($\boldsymbol{k}$) is most valuable, but the bulk flow ($\boldsymbol{V}$) is considerably less than the ion thermal speed ($\boldsymbol{v}_{\rm thi}$), so one cannot apply the Taylor condition (Taylor 1938). However, using delays on the measured $\boldsymbol{E}$ between the four spacecraft, we found that the structures (or waves) have a common speed.

Figure 3(a) displays a histogram of the speed of $\boldsymbol{E}$ structures (or waves) using time delays between four spacecraft. In this analysis, $\boldsymbol{E}$ is filtered to a frequency range $f > 0.25$ Hz, which eliminates most of the power at the ion cyclotron frequency ($\langle f_{\rm ci}\rangle \sim 0.15$ Hz). The time delays of 4 s intervals of $\boldsymbol{E}$ between MMS1 and the other spacecraft (see Figure 1(j)) is determined via cross-correlation, from which a velocity is calculated. Only events with high correlation coefficients (>0.8) and peak amplitudes of $|E_{\rm peak}| > 5$ mV m^{-1} are used. Often, those with $|E_{\rm peak}| < 5$ mV m^{-1} have low correlation coefficients, so the two criteria have a large overlap. The results indicate that the directions of the velocities are nearly random. However, the speeds of over 90% of the events are confined to between 1000 and 2800 km s^{-1} with an average of ~1890 km s^{-1}. An analysis of $\boldsymbol{B}$ (full bandwidth) yields similar results. This speed is between the Alfvén speed (V_A) and the ion acoustic speed (V_S; Figure 1, bottom right). As such, we directly translate the PSD of $\boldsymbol{B}$ and $\boldsymbol{E}$ from a function of f to a function of $|\boldsymbol{k}|\rho_i$, realizing that, since the speeds vary by a factor of 2 and ρ_i also varies, there is a factor of 2 blurring of the PSD.

Figures 3(c) and (d) display, respectively, the PSDs of $\boldsymbol{B}$ and $\boldsymbol{E}$ averaged over the entire interval of turbulent region 1. The lower horizontal axis shows f, which is the native calculation of the PSDs. The upper horizontal axis is $|\boldsymbol{k}|\rho_i$, which is a simple linear transformation using a speed of 1890 km s^{-1}. The PSD of $\boldsymbol{B}$ has a classic signature of plasma turbulence. At $|\boldsymbol{k}|\rho_i < 1$, the spectral index is consistent with –5/3. At $|\boldsymbol{k}|\rho_i > 1$, the spectral index noticeably steepens.

The PSD of $\boldsymbol{E}$ shows common signatures of turbulence in the magnetosphere (Ergun et al. 2015; Stawarz et al. 2016). The spectral index of $\boldsymbol{E}$ is shallower than that of $\boldsymbol{B}$ when $|\boldsymbol{k}|\rho_i < 1$. This shallow spectral index is interpreted as the buildup of kinetic Alfvén wave or fast-mode activity. Between $|\boldsymbol{k}|\rho_i > 1$ and $|\boldsymbol{k}|\rho_e < 1$ (or $|\boldsymbol{k}|d_e < 1$), the spectral index is shallower than −1, indicating a strong buildup of electrostatic energy at higher frequencies. It is important to realize that there is little stored energy in $\boldsymbol{E}$ (when compared to $\boldsymbol{B}$). Instead, the PSD of $\boldsymbol{E}$ is an indicator of the ability to transfer energy from electromagnetic fields to particles. When $|\boldsymbol{k}|\rho_e > 1$ and $|\boldsymbol{k}|d_e > 1$, the spectral index steepens.

The waveforms of $\boldsymbol{B}$ and $\boldsymbol{E}$ confirm that a variety of plasma structures are embedded in the turbulence (Stawarz et al. 2015; Ergun et al. 2015). These structures include magnetic holes (e.g., Goodrich et al. 2016), double layers (Ergun et al. 2009), electron phase-space holes (Andersson et al. 2009), and narrow current sheets, which suggest intermittency in turbulence. Statistically, intermittency should render non-Gaussian probability distribution functions (PDFs) of increments of $\boldsymbol{B}$ at small scales that become more Gaussian at larger scales:

$$\triangle B = B(t) - B(t - t_{\rm lag}). \quad (2)$$

Figure 3(b) plots the kurtosis (fourth-order moment divided by the square of the second-order moment) of the distribution of increments of $\boldsymbol{B}$ as a function of time lag. A kurtosis of 3 indicates a Gaussian PDF. Two of the PDFs of the increments of $\boldsymbol{B}$ are embedded in the plot, one with 1 s lag and one with 10 s lag. The kurtosis signifies non-Gaussian behavior at low time lags (<10 s), which indicates that intermittent structures dominate at short timescales. The PDFs of the increments of $\boldsymbol{B}$ relax to a kurtosis of 3 (Gaussian behavior) above 10 s.

The properties of the $\boldsymbol{E}$ turbulence are displayed in Figures 3(e)–(g). It is important to understand whether $\boldsymbol{E}$ is dominated by waves (correlated) or intermittent (uncorrelated) and possibly nonlinear plasma structures. The autocorrelation of E_x, filtered to $f > 0.25$ Hz, is displayed in Figure 3(e). One can see that the E_x with $f > 0.25$ Hz has a well-defined correlation time of $t_c = 24$ ms. The exponential fit (e^{-t/t_c}; gold line) lies on top of the autocorrelation of E_x from each of the four MMS spacecraft. The low-frequency cutoff of 0.25 Hz is chosen, as it represents a clear break in the correlation time. If one isolates the frequencies below 0.25 Hz (not shown), the correlation time expands to over 1 s, suggesting the lower-frequency $\boldsymbol{E}$ may be dominated by plasma waves.

The black dots in Figure 3(f) represent six cross-correlation values from the four MMS spacecraft. The distances between the spacecraft, given in Figure 1(j), range from ~12.4 to ~19.6 km. In Figure 3(e), the distances are translated into time by dividing them by 2000 km s^{-1}, which is nearly the same as the average speed of $\boldsymbol{E}$ structures. Figure 3(f) is an expanded view of the cross-correlations as a function of distance. The gold line is an exponential fit (e^{-d/d_c}). The fit indicates a correlation distance (d_c) of ~48 km, which is in excellent agreement with the calculated $d_c \sim 45$ km using the product of the correlation time (24 ms) and average structure speed (1890 km s^{-1}). This analysis is repeated for E_y with similar results. Although E_z is measured by shorter antennas (Ergun et al. 2016), it also suggests similar correlation values. One clear conclusion is that $\boldsymbol{E}$ with $f > 0.25$ Hz is dominated by intermittent structures with a well-defined correlation time (24 ms) and an associated correlation distance (~48 km).

Figure 3(g) displays a PDF of $|\boldsymbol{E}|$ ($f > 0.25$) for turbulent region 1. The black line is the PDF, and the blue line is a fit. This PDF is puzzling, as it does not appear to be a Gaussian or

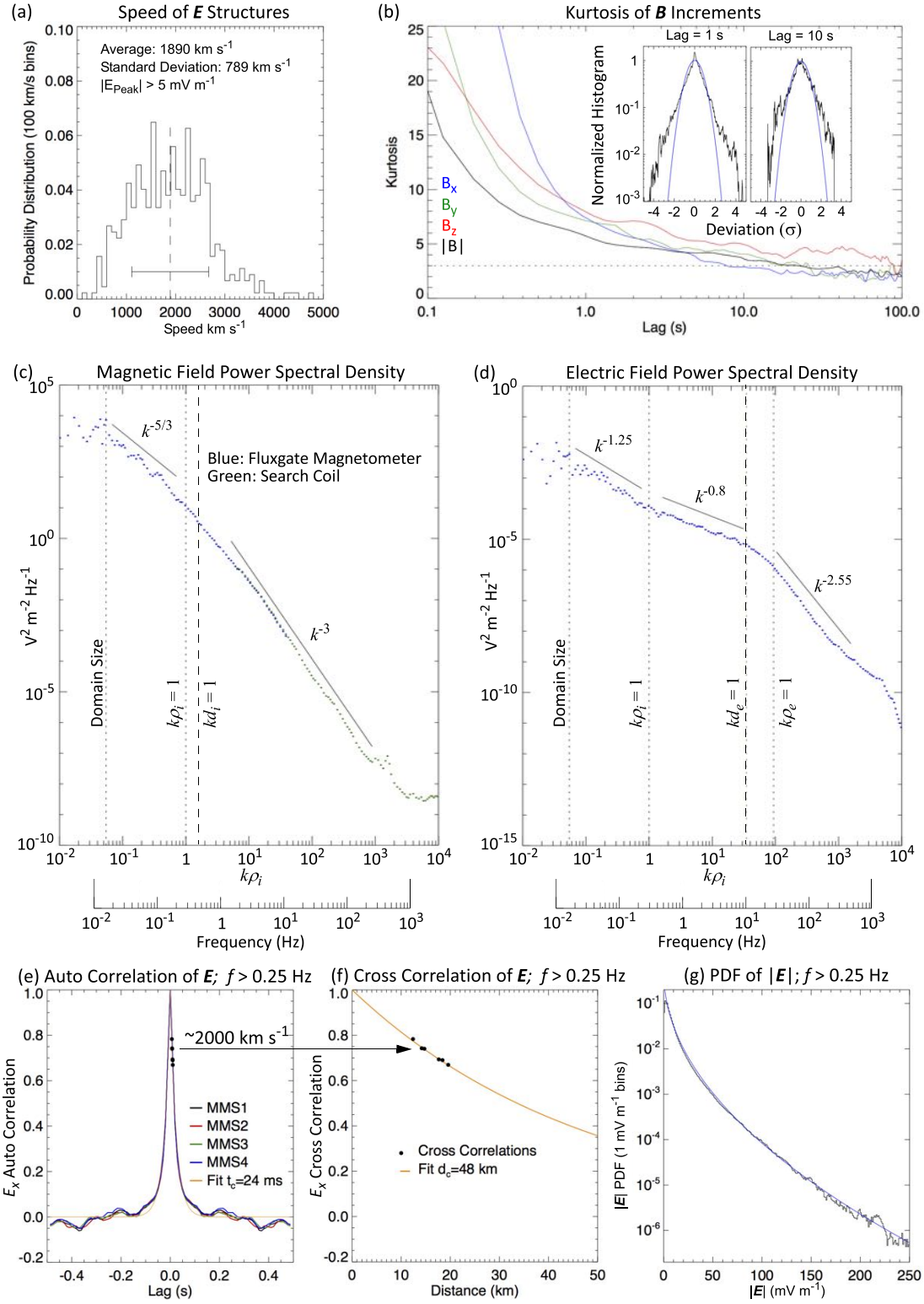

Figure 3. Properties of $\boldsymbol{E}$ and $\boldsymbol{B}$ in strong turbulence. (a) Histogram of the speed of $\boldsymbol{E}$ structures; $\boldsymbol{E}$ is filtered to frequencies >0.25 Hz. A velocity is determined from time delays between 4 s intervals that are calculated via cross-correlation. Events with a high correlation coefficient (>0.8) and amplitudes greater than 5 mV m^{-1} are used to make the histogram. The directions are nearly random. The average speed is 1890 km s^{-1}. (b) Kurtosis of increments of $\boldsymbol{B}$ as a function of lag time. The colors represent components. The kurtosis relaxes to 3 (Gaussian distribution) at greater than ∼10 s lag. Distributions at 1 and 10 s lag are included in the plot. (c) PSD of $\boldsymbol{B}$ as a function of $|\boldsymbol{k}|\rho_i$ and frequency (lower axis). The PSD is calculated as a function of frequency using a pseudo log-spaced FFT algorithm and translated to a function of $|\boldsymbol{k}|\rho_i$ (ρ_i is given in the table in Figure 1) assuming a structure speed of 1890 km s^{-1}. The vertical dashed lines show the domain size (10^8 m), $|\boldsymbol{k}|\rho_i = 1$, and $|\boldsymbol{k}|d_i = 1$. The solid black lines are for visual reference; they are not fits. (d) PSD of $\boldsymbol{E}$ as a function of $|\boldsymbol{k}|\rho_i$ and frequency (lower axis). The PSD is calculated with the same algorithm used for the PSD of B. The vertical dashed lines show the domain size (10^8 m), $|\boldsymbol{k}|\rho_i = 1$, $|\boldsymbol{k}|d_e = 1$, and $|\boldsymbol{k}|\rho_e = 1$. The solid black lines are for visual reference; they are not fits. (e) Autocorrelation of E_x (8192 samples s^{-1} and filtered to $f > 0.25$ Hz) as a function of lag time. The colors represent the four spacecraft. The gold line represents a fit to an exponential (e^{-t/t_c}) with $t_c = 24$ ms. (f) Expanded view (six black dots) of the cross-correlation E_x ($f > 0.25$ Hz) between each the spacecraft. The distances between the spacecraft are given in Figure 1(j). The gold line is an exponential with a correlation distance of 48 km. (g) PDF of $|\boldsymbol{E}|$ for $f > 0.25$. The PDF fits remarkably well to a stretched exponential, $e^{-\sqrt{|E|/E_0}}$, where $E_0 = 1.3$ mV m^{-1}.

a power-law function. Instead, the PDF fits well to a stretched exponential,

$$\mathrm{P}(|\mathrm{E}|) \propto e^{-\sqrt{|E|/E_0}}, \quad (3)$$

where $E_o = 1.3\,\mathrm{mV\,m^{-1}}$. Such a distribution has no clear mathematical basis that is known to the authors. The PDF has a sharp peak near $|\boldsymbol{E}| = 0$. The high-amplitude range has a non-Gaussian tail. Although there is no immediate justification, the remarkably good functional fit of the PDF, along with the defined values of t_c and d_c, permits one to model $\boldsymbol{E}$ in strong turbulence.

The statistical analysis of $\boldsymbol{B}$ and $\boldsymbol{E}$ supports the initial supposition of strong, intermittent turbulence. Of significance, the reasonably well-defined correlation time and distance indicate that $\boldsymbol{E}$ with $f > 0.25$ Hz is not well described as a mixture of linear waveforms. Instead, $\boldsymbol{E}$ ($f > 0.25$ Hz) is better represented by a set of pseudorandom fluctuations. The functional form of the PDF of $\boldsymbol{E}$, while puzzling, allows one to reproduce or analyze $\boldsymbol{E}$. On the other hand, $\boldsymbol{E}$ with $f < 0.25$ Hz may be dominated by coherent waves.

2.3. Observations of Electron Heating and Acceleration

Figure 1 shows a large-scale (roughly 16 R_E) association between $\boldsymbol{B}$ and $\boldsymbol{E}$ turbulence and particle heating and acceleration. Figure 2 suggests that this heating and acceleration ultimately involve annihilation of magnetic energy that is enabled by magnetic reconnection. Figure 3 describes the properties of $\boldsymbol{E}$ and $\boldsymbol{B}$. In this section, we examine the particle heating closely to determine how electromagnetic energy is converted into particle energy and nonthermal tails form on the particle distributions. In an early study (Ergun et al. 2018), $\boldsymbol{J}\cdot\boldsymbol{E}$ was examined; it was found that the primary energy conversion is by perpendicular $\boldsymbol{E}$.

We begin studying acceleration by examining the energetic electrons. Figures 4(a) and (b) display a 6 s period inside of turbulent region 1 of the energetic electron fluxes (60 to ~500 keV) and thermal electrons (~10 eV to ~25 keV). From visual examination of Figure 4(a), one can see that the energetic electron fluxes at ~100 keV often occur in bursts of 1–5 s. The rapid increases and decreases of fluxes over a large energy range (60 to >200 keV) most often show no dispersion (time delays), which indicates a local acceleration or trapping mechanism. These events are studied in detail.

The "acceleration events" that are marked at the top of Figure 4 are determined by an algorithm that is based solely on energetic electron fluxes. A weighted time series of electron fluxes emphasizes the fluxes in the 60–250 keV energy range,

$$F_W(t) = \sum_{60\mathrm{keV}}^{250\mathrm{keV}} W_E F_E(t), \quad (4)$$

where F_E is the electron flux in each energy bin and W_E is a normalized weight assigned to each energy bin. Here $\langle F_W\rangle$ is smoothed over 15 s. An event is identified if the peaks of $F_W - \langle F_W\rangle$ exceed two times $\langle F_W\rangle$. The beginning and end of the event are selected when the fluxes return to less than 1.25 times $\langle F_W\rangle$. This algorithm identified 42 acceleration events. It is designed to identify a representative set of enhanced energetic electron events based solely on the amplitude of electron fluxes so that the low-enegery properties of the particle distributions, $\boldsymbol{B}$, $\boldsymbol{E}$, and $\boldsymbol{J}\cdot\boldsymbol{E}$ can be objectively examined.

We begin with events 8 and 9, which have features seen in more than half of the acceleration events. Figures 4(c) and (d) plot, respectively, the energetic electron fluxes and thermal electrons over a 10 s interval, during which there are two acceleration events. Event 8 is from ~07:27:31.4 to ~07:27:33.3 UT, and event 9 is from ~07:27:34 to ~07:27:36.2 UT. Dark green bars between panels (c) and (d) and above panel (h) mark the events. Figure 4(e) indicates that events occur at the beginning and end of a depletion in $|\boldsymbol{B}|$. Here $\boldsymbol{E}$ is active during the events with amplitudes $>40\,\mathrm{mV\,m^{-1}}$ (Figure 4(f)).

The perpendicular contribution to $\boldsymbol{J}\cdot\boldsymbol{E}$ (Figure 4(g), blue line) shows a positive average of ~0.2 nW $\mathrm{m^{-3}}$ (~40 keV $\mathrm{s^{-1}}$ per particle pair) before, during, and after the events. The parallel contribution to $\boldsymbol{J}\cdot\boldsymbol{E}$ (Figure 4(g), red line) has a considerably lower contribution. In an earlier study (Ergun et al. 2018), $\boldsymbol{J}\cdot\boldsymbol{E}$ is evaluated to have a strong contribution of $\langle\boldsymbol{J}\rangle\cdot\langle\boldsymbol{E}\rangle/\langle n\rangle > 1$ keV $\mathrm{s^{-1}}$ per particle pair. Baseline offsets in $\boldsymbol{E}$ dominate the uncertainty. After a recalibration of $\boldsymbol{E}$, the full value of $\langle\boldsymbol{J}\cdot\boldsymbol{E}\rangle/\langle n\rangle$ is determined to be ~3.4 ± 1 keV $\mathrm{s^{-1}}$ per particle pair. This value compares well to the estimated Poynting flux entering the turbulent region (~1.5–3.0 keV $\mathrm{s^{-1}}$ per particle pair; see earlier). A notable feature in examining Figure 4(g) is that $\boldsymbol{J}\cdot\boldsymbol{E}$ is elevated over 10 times its average during acceleration events 8 and 9.

Three of 15 high-energy channels of electron fluxes are displayed in Figures 4(h)–(j). These panels plot intensity as a function of pitch angle and time. Both events have enhanced fluxes at 70 (Figure 4(h)) and 106 (Figure 4(i)) keV that are primarily at perpendicular pitch angles (45°–135°). The black lines separate the population of electrons that are possibly trapped in a magnetic depletion from the free electrons (not trapped) using the local value of $|\boldsymbol{B}|$ compared to a maximum $|\boldsymbol{B}|$ of 17 nT in the plot. The energetic electrons appear to be trapped.

The electron distribution function for event 9 is displayed in Figure 4(k). Blue squares are from the FPI (10 eV–25 keV) averaged over all directions. The red circles are from the EPD averaged over all directions. A Maxwellian function representing a 4.7 keV thermal core (black line; not a fit) is plotted for reference (the 4.7 keV value is explained later). The distribution in Figure 4(k) is non-Maxwellian. Rather, the phase-space density is nearly flat below ~18 keV. At the 18 keV shoulder, the phase-space density drops abruptly.

Figure 4(l) describes the 2D (reduced) low-energy (~10 eV to ~25 keV) distribution during event 9. The horizontal axis is the parallel velocity ($V_\parallel$), and the vertical axis is one of the perpendicular velocities ($V_\perp$). The dashed circle (15 keV) is for visual reference. One can see from the oblong shape of the 2D electron distribution that the parallel electron temperature is enhanced over the perpendicular electron temperature in the low-energy electrons. To the contrary, high-energy electrons have enhanced perpendicular energy.

Figure 4(m) replots the omnidirectional electron intensity (or flux) as a function of energy, which is a more usual format when studying acceleration. This format is used in subsequent figures. Figure 4(n) plots the electron intensity from a "quiet" period after the event. Comparing the two intensity plots reveals that the acceleration process in event 9 enhances the ~10 to ~150 keV electron fluxes over a heated 4.7 keV thermal core (Figure 4(n)). (The T_e outside of the large-scale turbulent region is ~1 keV).

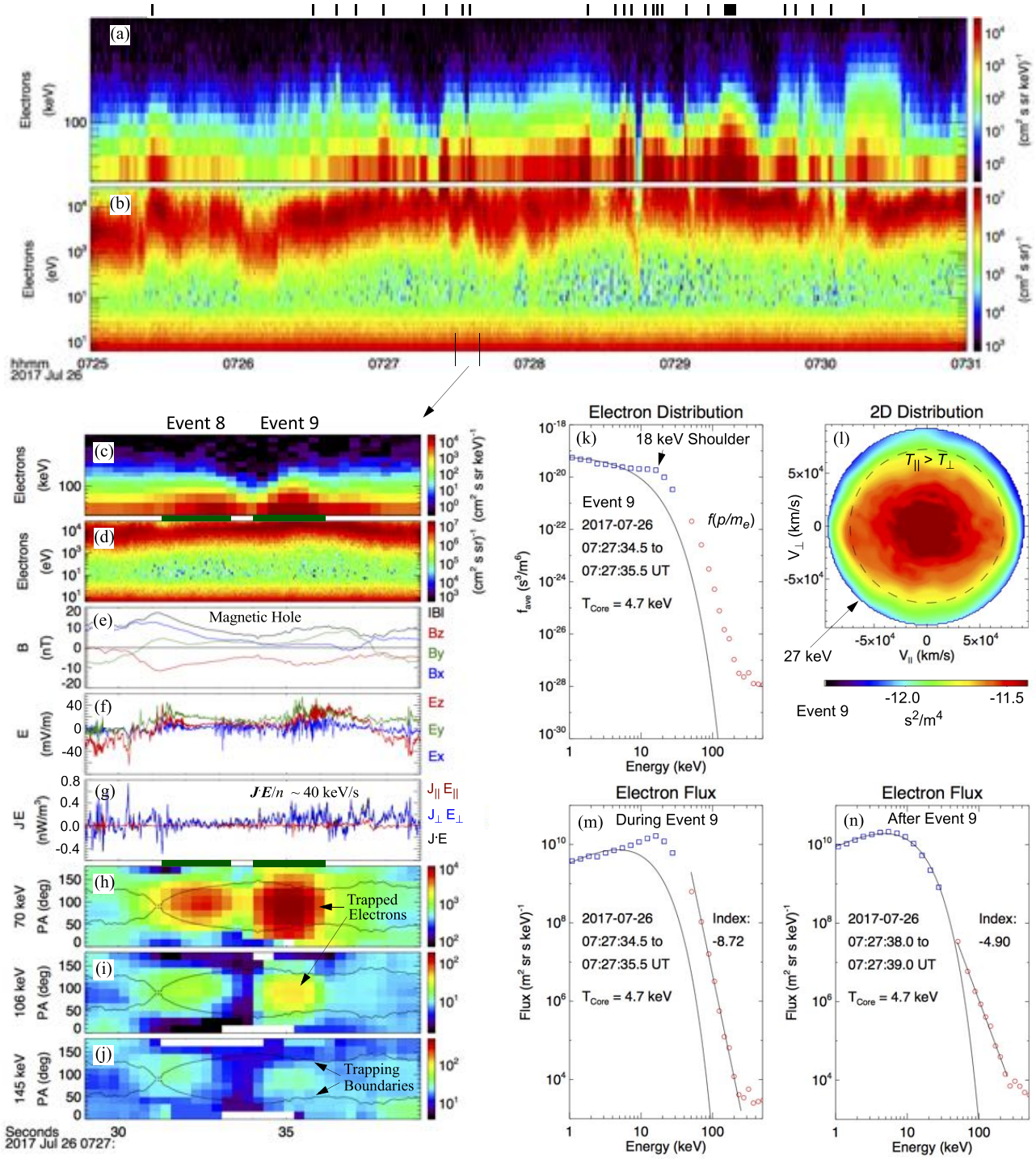

Figure 4. Electron acceleration events 8 and 9. (a) Omnidirectional electron flux as a function of energy and time. The energy range is from 50 to 500 keV. The marks at the top of the panel are identified acceleration events. (b) Electron differential energy flux in the energy range from 10 eV to 25 keV. (c) Electron flux in the energy range from 50 to 500 keV during events 8 and 9. (d) Electron differential energy flux in the energy range from 10 eV to 25 keV. (e) $\boldsymbol{B}$ at 8192 samples s^{-1}. (f) $\boldsymbol{E}$ at 8192 samples s^{-1}. (g) $\boldsymbol{J} \cdot \boldsymbol{E}$. Here $\boldsymbol{J}$ is calculated via the curlometer technique ($\nabla \times \boldsymbol{B}$ from four spacecraft; Dunlop et al. 2002). The red line is the parallel contribution, the blue line is the perpendicular contribution, and the black line is the total. (h) Electron flux as a function of pitch angle and time for electrons of energies between ~62 and ~77 keV. The black lines represent trapping boundaries. (i) Electron flux as a function of pitch angle and time for electrons of energies between ~94 and ~117 keV. (j) Electron flux as a function of pitch angle and time for electrons of energies between ~130 and ~160 keV. (k) Electron distribution as a function of energy (averaged over pitch angle) from 07:27:34.5 to 07:27:35.5 UT, which is the period of event 9. The blue squares are from the FPI. The red circles are from the EPD instrument. The black line represents a Maxwellian with $T_e = 4.7$ keV. (l) 2D electron distribution from 10 eV to ~25 keV. The vertical axis has a velocity direction perpendicular to $\boldsymbol{B}$, and the horizontal axis has a velocity direction parallel to $\boldsymbol{B}$. The dashed circle (15 keV) highlights that $T_{e\|} > T_{e\perp}$ for the low-energy core. (m) Electron flux as a function of energy during event 9. The blue squares are from the FPI. The red circles are from the EPD instrument. The curved black line represents a Maxwellian with $T_e = 4.7$ keV. The straight black line is a power-law fit to the high-energy tail. (n) Electron flux as a function of energy after event 9.

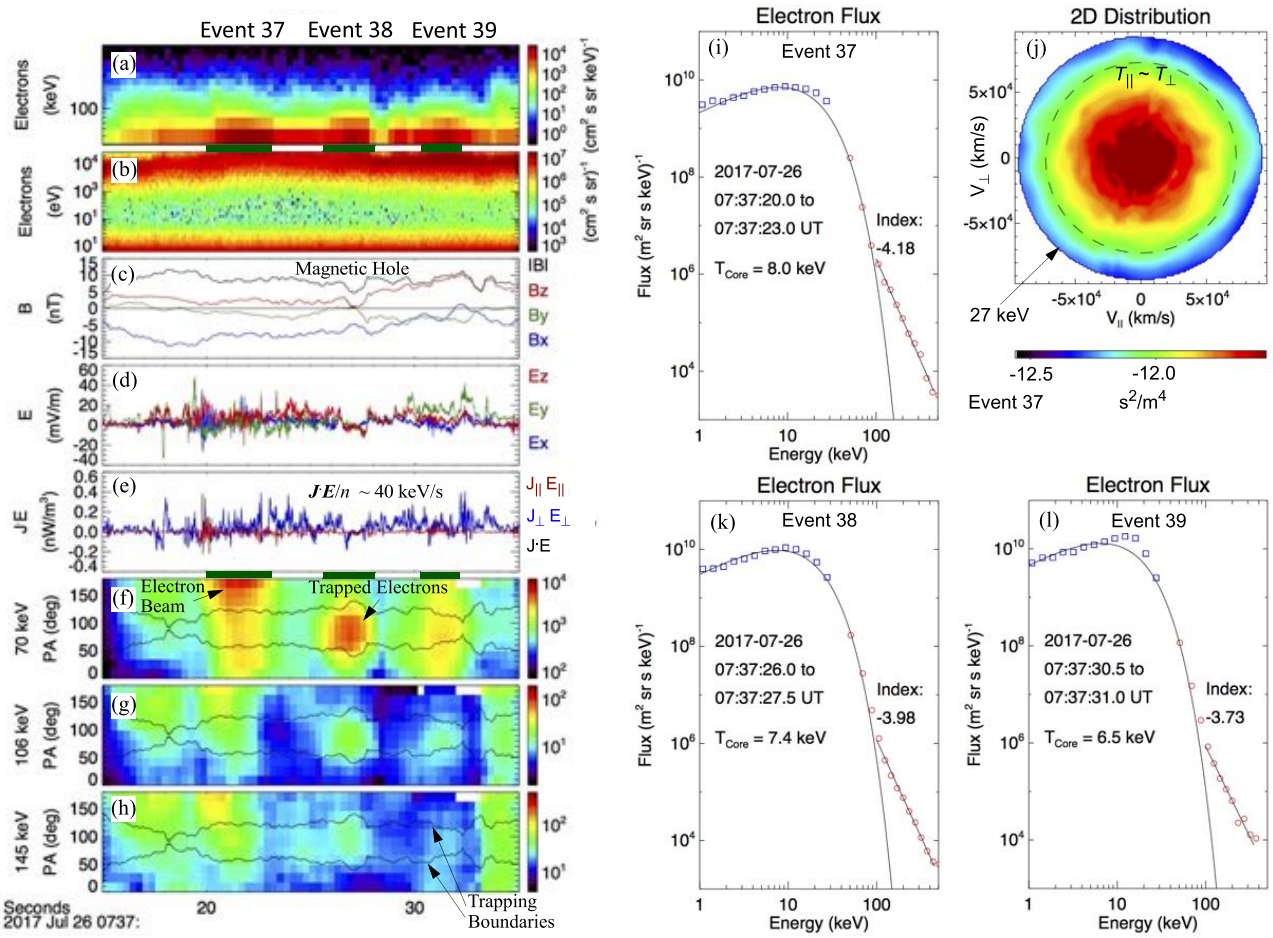

Figure 5. Electron acceleration events 37, 38, and 39. (a) Electron flux in the energy range from 50 to 500 keV. (b) Electron differential energy flux in the energy range from 10 eV to 25 keV. (c) $\boldsymbol{B}$ at 8192 samples s^{-1}. (d) $\boldsymbol{E}$ at 8192 samples s^{-1}. (e) $\boldsymbol{J} \cdot \boldsymbol{E}$. (f) Electron flux as a function of pitch angle and time for electrons of energies between ~62 and ~77 keV. The black lines represent trapping boundaries. (g) Electron flux as a function of pitch angle and time for electrons of energies between ~94 and ~117 keV. (h) Electron flux as a function of pitch angle and time for electrons of energies between ~130 and ~160 keV. (i) Electron flux during event 37. The time is marked on the plot. (j) 2D electron distribution during event 37. (k) Electron flux during event 38. (l) Electron flux during event 39.

While the features in events 8 and 9 are observed in many events, the electron distributions during some acceleration events can be substantially different. Figure 5 displays three more acceleration events that are late in the large-scale turbulent region. At that time, the electron temperatures are higher than early in the event, and the energetic electrons are more continuously observed (Figure 1).

The format of Figure 5 is nearly identical to that of Figure 4, so our description of the plots is brief. The three events are marked with dark green bars and labeled at the top of the plot. The black line, $|\boldsymbol{B}|$, in Figure 5(c) is slightly below its maximum during event 37, shows a magnetic depletion during event 38, and is near its maximum value (but varying) during event 39. Throughout the interval in Figure 5, $\boldsymbol{E}$ (Figure 5(d)) is fluctuating with peaks of tens of mV m^{-1}, and $\boldsymbol{J} \cdot \boldsymbol{E}$ (Figure 5(e)) is mostly positive, averaging ~25 keV s^{-1} per particle pair. Interestingly, the parallel contribution of $\boldsymbol{J} \cdot \boldsymbol{E}$ is strong at the beginning of event 37.

The energetic electrons in event 37 (Figures 5(f)–(h)) appear as a beam near 180° pitch angle, which is traveling earthward, since B_x (Figure 5(c)) is negative at that time. Since the turbulent region is mostly tailward of MMS (see Figure 1), the beam is emerging from the turbulent region. The 1 to ~100 keV fluxes shown in Figure 5(i) (averaged over all angles) are nearly Maxwellian with $T_e \sim 8$ keV. The energetic tail has a power-law index of roughly −4. Oddly, the low-energy electrons indicate that $T_{e\parallel} \sim T_{e\perp}$, even though the energetic electrons are mainly parallel to $\boldsymbol{B}$. Importantly, the 145 keV electrons in event 37 (Figure 5(h)) arrive before the 70 keV electrons (Figure 5(f)). If from the same source, the ~1 s delay indicates the source is roughly 10 R_E from the observing point; 10 R_E is within the large-scale turbulent region. Such dispersion, while interesting, is rarely seen in the identified events.

The energetic electrons (Figures 5(f)–(h)) in event 38 appear to be trapped, as in event 9. Unlike event 9, the 1 to ~100 keV fluxes are nearly Maxwellian with $T_e \sim 7.4$ keV, $T_{e\parallel} \sim T_{e\perp}$, and the energetic tail has a power-law index of approximately −4. The energetic electrons (Figures 5(f)–(h)) in event 39 have a slightly enhanced trapped population but are otherwise more isotropic in pitch angle. The fluxes in event 39 (Figure 5(l)) do not appear to be Maxwellian. Rather, they have a shoulder at ~15 keV.

Even though there are variations, several patterns emerge when all 42 acceleration events are examined. (1) A majority (~85%) of the acceleration events are seen inside of a magnetic depletion. (2) The fluctuations in $\boldsymbol{E}$ have amplitudes that exceed tens of mV m^{-1} in all of the events. (3) In all but one of the events, $\boldsymbol{J} \cdot \boldsymbol{E}$ is net positive. In all but five of the events (88%), $\boldsymbol{J} \cdot \boldsymbol{E}$ noticeably increased (by a factor of 3, on average)

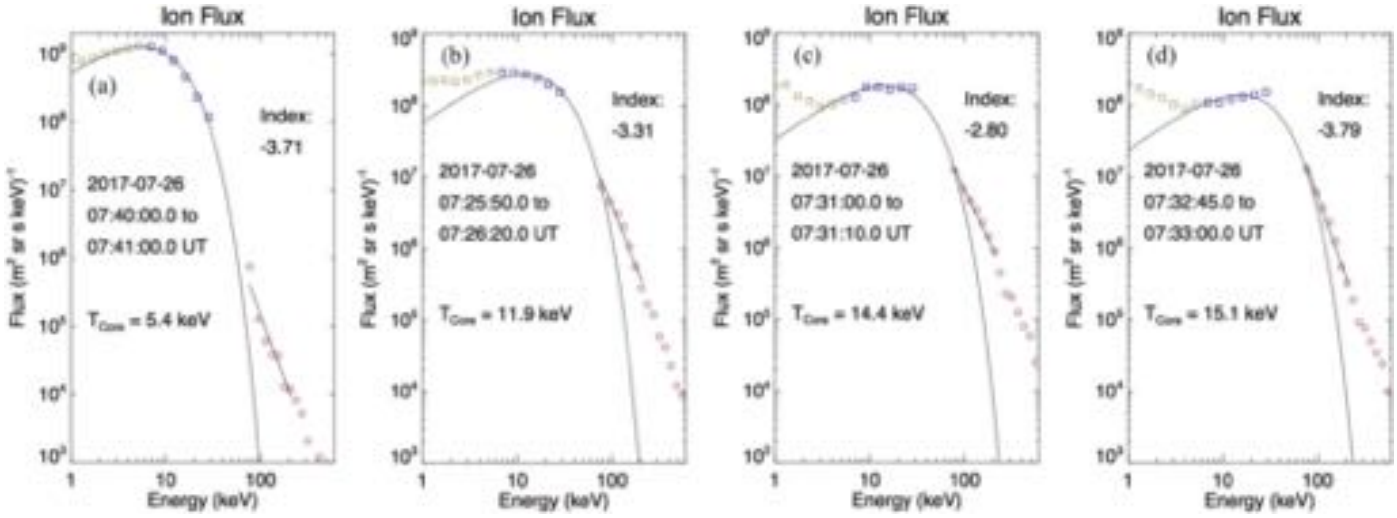

Figure 6. Ion fluxes. (a) Ion fluxes between turbulent regions 1 and 2. The blue squares are from the FPI, and the red circles are from the EPD instrument. The yellow squares indicate possible contamination from energetic electrons. The black lines are a Maxwellian fit to the thermal core and a power-law fit to the higher-energy tail. (b)–(d) Ion intensities inside of turbulent region 1. The time periods and fit parameters are on the plot.

over the average of $\boldsymbol{J} \cdot \boldsymbol{E}$ in the large-scale turbulent region. The perpendicular contribution of $\boldsymbol{J} \cdot \boldsymbol{E}$ dominates over the parallel contribution. (4) In the majority of the events, the highest-energy electrons (>70 keV) have enhanced perpendicular fluxes that appear to be trapped. (5) To the contrary, the thermal core of the electrons most often has $T_{e\|} \geqslant T_{e\perp}$. (6) In many of the events, a non-Maxwellian shoulder is seen in the 10–20 keV energy range. (7) The acceleration events with trapped electrons (and some with beam-like energetic electrons) rarely show observable dispersion (delays in the arrival time of the lower-energy electrons).

Given that the selection algorithm of the 42 acceleration events is based solely on energetic electron fluxes, one can come to several solid conclusions. (1) The energetic electrons are locally heated and accelerated inside of the large-scale turbulence. (2) Trapping by magnetic holes or depletions in $|\boldsymbol{B}|$ appears to play a strong role in the acceleration of the high-energy (nonthermal) electrons. (3) The strong fluctuations of $\boldsymbol{E}$ embedded in the turbulence appear to transfer magnetic energy to the particles through the perpendicular contribution of $\boldsymbol{J} \cdot \boldsymbol{E}$.

2.4. Observations of Ion Heating and Acceleration

Ions appear to absorb the majority of the electromagnetic energy that is transferred to the particles through $\boldsymbol{J} \cdot \boldsymbol{E}$. As a result, the ion temperatures (T_i) reach, on average, approximately 20 keV (second moment of the full distribution), which is significantly higher than T_e. Ion energization also appears to have variation (Figure 1). Flux enhancements are of the order of ~10 s and appear to endure longer than the electron flux enhancements. At high resolution, ion and electron flux enhancements are not always concurrent. Figure 1 shows a clear correlation between ion energization and turbulence on large scales.

As pointed out in earlier studies (Speiser 1965), ions in a reversing magnetic field such as Earth's magnetotail can flow in the Y-direction (out of plane in Figure 2) with quasi-adiabatic and/or chaotic orbits. These ions carry current and can gain energy due to the out-of-plane electric field, E_y. Finite B_z limits the energy gain of an individual ion. While there is no doubt significant ion energization due to this process, our investigation aims to understand the enhancement of energetic ion fluxes coincident with $\boldsymbol{E}$ and $\boldsymbol{B}$ turbulence.

Figure 6 displays ion intensity plots for one interval outside of the turbulent region and three intervals of enhanced ion fluxes inside of turbulent region 1 (Figure 1). We begin with a 1 minute interval outside of the turbulent region (Figure 6(a)). Ion intensity plots are compiled over intervals of tens of seconds to improve statistical accuracy and, for the EPD, angular coverage. Figure 6(a) shows the ion intensity in an interval between turbulent regions 1 and 2. As earlier, the blue squares are from the FPI, and the red circles are from the EPD. The specific EPDs used for Figure 6 do not discriminate the mass (species) of ions (Blake et al. 2016). The black lines are a Maxwellian fit to the thermal core and a power-law fit to the higher-energy tail. Ion count rates below ~5 keV (yellow squares) are very low and may be contaminated by energetic electrons that penetrate the analyzer, so these fluxes are not included in determining the core value of T_i. The thermal core appears Maxwellian with $T_i \sim 5.7$ keV.

Figure 6(a) indicates a low-intensity tail with a power-law index of approximately –3.7 for energies between 80 and 200 keV, which is likely from ions escaping the nearby turbulent regions. To properly interpret the high-energy ions in Figure 6, one must consider ion mass. When time-averaged over long periods (many minutes), mass-resolved observations (Cohen et al. 2017) indicate that ion fluxes with energies below ~200 keV are predominantly protons; little proton flux is seen above ~300 keV in this event. The highest-energy ions are He^{++} and O^{6+} from the solar wind, which can penetrate into the magnetotail gaining energies of roughly $q\int \boldsymbol{E} \cdot d\boldsymbol{l}$ (q is charge and $d\boldsymbol{l}$ is the path in the magnetotail; see Cohen et al. 2017). At energies greater than ~200 keV, heavy solar wind ion fluxes can exceed proton fluxes, so fluxes with energies above 200 keV are not used in our fits.

Figure 6(b) displays the ion intensity during a 30 s energetic ion flux enhancement from 07:25:50 to 07:26:20 UT, which is early in turbulent region 1. At the same time, there was a long-duration (~30 s) and possibly large-scale depression in $|\boldsymbol{B}|$, so ion trapping is possible. Pitch angle distributions of energetic ions cannot be accurately derived from the available data, so trapping cannot be verified. During this period, there is an increase in the perpendicular contribution of $\boldsymbol{J} \cdot \boldsymbol{E}$ but no electron acceleration

event. The ion fluxes in Figure 6(b) have a thermal core with $T_i \sim 11.9$ keV and an energetic, nonthermal tail with a power-law index of approximately −3.3. The nonthermal tail in Figure 6(b) has 10 times higher intensity than that in Figure 6(a). Here T_i calculated as the second moment of the distribution is ∼18 keV.

Figure 6(c) displays one of the most intense 10 s periods of energetic ion fluxes inside of turbulent region 1. The thermal core temperature is roughly 14–16 keV (the core fit is poor), and the energetic, nonthermal tail hardens with a power-law index of −2.8. These enhanced ion fluxes are inside of a deep depression in $|\boldsymbol{B}|$ ($|\boldsymbol{B}| \sim 3$ nT) and coincident with very large, positive $\boldsymbol{J} \cdot \boldsymbol{E}$. An electron acceleration event was concurrent. Figure 6(d) displays a third period of enhanced, energetic ion fluxes later in the turbulent region. Again, the enhanced ion fluxes are inside of a deep depression in $|\boldsymbol{B}|$ and coincident with very large, positive $\boldsymbol{J} \cdot \boldsymbol{E}$. In this latter event, the fit to a thermal core is poor. Instead, the ion fluxes appear to have an enhanced shoulder that was seen in many of the electron flux plots.

When compared to the ion fluxes outside of the turbulent region (Figure 6(a)), the ion fluxes inside of the turbulent region (Figures 6(b)–(d)) are clearly heated and accelerated. The power-law indices of the energetic ions remain fairly hard (−2.8 to −3.8). Outside of the turbulent region, the accelerated tail has greatly reduced intensity, which indicates escaping ions from the turbulent region. On average, the ion temperatures (core and tail; second moment of the distributions) are estimated to be roughly 20 keV, which is several times T_i in the surrounding regions. The primary conclusions from the examination of ion distributions are that (1) ions are heated and nonthermally accelerated locally inside of turbulent region 1, (2) the acceleration process may involve trapping, and (3) heating and acceleration are associated with enhanced $\boldsymbol{J} \cdot \boldsymbol{E}$.

3. Acceleration Mechanisms

Acceleration mechanisms are difficult to isolate inside of a turbulent environment. We expect that part of the ion heating is from E_y combined with quasi-adiabatic and/or chaotic orbits in a reversing magnetic field (Speiser 1965). We suspect that cyclotron-resonant acceleration of ions (e.g., Chang et al. 1986), second-order acceleration of electrons, double layers (e.g., Ergun et al. 2009), wave–particle interactions, Fermi acceleration (Drake et al. 2006; Zank et al. 2014, 2015; Zhao et al. 2018, 2019), and magnetic pumping (betatron acceleration; e.g., Alfvén 1954) are all active.

Since ions carry the majority of the thermal energy, slow temporal variation in $|\boldsymbol{B}|$ should result in a change of perpendicular energy due to the conservation of the first adiabatic moment ($\mu = p_\perp^2/2m_i|\boldsymbol{B}|$). If the adiabatic moment is conserved, then $d\mu/dt = 0$, which implies

$$\mu \frac{d|\boldsymbol{B}|}{dt} = \frac{d(\langle p_\perp^2/2m_i \rangle)}{dt}, \tag{5}$$

and $\boldsymbol{J} \cdot \boldsymbol{E}/n$ is dominated by the perpendicular contribution. So, if parallel energy is ignored,

$$\frac{d(\langle p_\perp^2/2m_i \rangle)}{dt} \approx \frac{\boldsymbol{J} \cdot \boldsymbol{E}}{n}. \tag{6}$$

To examine whether magnetic pumping may be active, we compare $d|\boldsymbol{B}|/dt$ with $\boldsymbol{J} \cdot \boldsymbol{E}/n$. Both values can be directly derived from the data.

Figure 7 plots measured values of $d|\boldsymbol{B}|/dt$ and $\boldsymbol{J} \cdot \boldsymbol{E}$ at ∼8 ms intervals (black dots) inside of turbulent region 1. The gold dots with error bars are averages over 1 nT s^{-1} bins. The blue line is a linear fit. There is a significant positive slope (∼5×10^{-3} J m^{-3} T^{-1}) signifying possible magnetic pumping. Under adiabatic behavior, this slope should be equal to $\mu\langle n \rangle$. Using $\langle |\boldsymbol{B}| \rangle \approx 10$ nT, $\langle n \rangle \approx 0.03$ cm^{-3}, and $\langle p_\perp^2/2m_i \rangle \approx 20$ keV, we estimate $\mu\langle n \rangle \approx 9 \times 10^{-3}$ J m^{-3} T^{-1}. Given the uncertainties of the values, the measured slope is consistent with that expected from adiabatic behavior.

The data in Figure 7 imply that variations in $|\boldsymbol{B}|$ on timescales longer than $1/f_{ci}$ are embedded in the turbulence. However, this correlation certainly does not rule out fast changes in $|\boldsymbol{B}|$, cyclotron-resonant heating, Fermi acceleration, or other energization mechanisms. We point out that magnetic pumping (adiabatic behavior) by itself does not energize a plasma unless the particles evolve to a permanently higher $|\boldsymbol{B}|$ or some scattering process is involved (e.g., Alfvén 1954). In turbulence, the background magnetic field does not necessarily permanently increase or decrease. However, magnetic pumping can nonlinearly enhance another energization process; heating in a low $|\boldsymbol{B}|$ region can be greatly amplified (e.g., Lichko et al. 2017). Furthermore, Fermi acceleration from collapsing mirrors (Drake et al. 2006; Zank et al. 2014, 2015; Zhao et al. 2018, 2019) would also produce a similar relation between $\boldsymbol{J} \cdot \boldsymbol{E}$ and $d|\boldsymbol{B}|/dt$. We hypothesize that several energization mechanisms may be active and that a primary effect of the depletions in $\boldsymbol{B}$ is trapping of ions.

4. Summary

The MMS spacecraft detected magnetic reconnection associated with strong turbulence and particle acceleration in the Earth's magnetotail. Magnetic reconnection is inferred from a velocity jet reversal combined with a reversal of B_z (Nagai et al. 1998; Øieroset et al. 2001; Torbert et al. 2018). The X-line retreats anti-earthward, allowing the MMS satellites to explore the large-scale turbulent region and the concomitant particle acceleration. We estimate the extent of the turbulent region to be of the order of 16 R_E (10^8 m) in the X-direction (Figure 2) and 2–4 R_E in the Z-direction. The extent in the Y-direction (along the X-line of the magnetic reconnections) is unknown.

In this particular turbulent region, the amplitudes of $\boldsymbol{E}$ fluctuations (>200 mV m^{-1}) exceed those expected from the flow velocities where $|\boldsymbol{V}_i \times \boldsymbol{B}| < \sim 20$ mV m^{-1}. The magnetic fluctuations are such that $|\delta\boldsymbol{B}|/|\boldsymbol{B}| \sim 1$, implying strong, localized currents, which is consistent with the intermittent nature of the turbulence (Figure 3(b)). Ions and electrons are heated to several times the ambient temperatures, and a fraction of them are accelerated to hundreds of kilovolts. The plasma density is lower in the region of turbulence.

The region of strong turbulence that engulfs the magnetic reconnection region occupies a much larger volume than does the diffusion region. Magnetic field energy builds in the lobes in the Earth's magnetotail due to subsolar magnetic reconnection (e.g., Dungey 1961) and is often violently released in near-Earth magnetic reconnection events. Magnetic field annihilation generates Poynting flux that enters the turbulent region from the lobes. Estimates of the Poynting flux entering turbulent region 1 (Figure 2) and direct measurements of $\langle \boldsymbol{J} \cdot \boldsymbol{E} \rangle$ are quantitatively consistent. While annihilation is enabled by magnetic reconnection, the aggregate energy release in the surrounding region is far greater than that in the diffusion

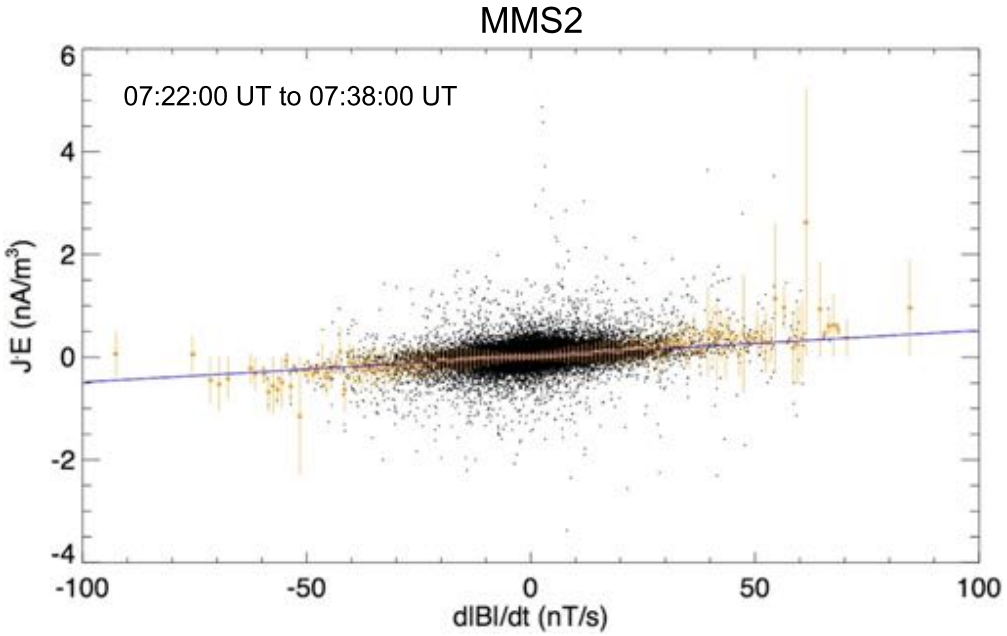

Figure 7. The $\boldsymbol{J}\cdot\boldsymbol{E}$ vs. $d|\boldsymbol{B}|/dt$ inside of turbulent region 1. The ~123,000 black dots are 8 ms increments of $\boldsymbol{J}\cdot\boldsymbol{E}$ vs. $d|\boldsymbol{B}|/dt$. The gold dots are $\langle \boldsymbol{J}\cdot\boldsymbol{E}\rangle$ in 1 nT s^{-1} bins. The error bars are based on the number of events and the uncertainty in $\boldsymbol{J}\cdot\boldsymbol{E}$. The positive slope of the fit (blue line) is significant.

region alone. The turbulence also erupts, in part, due to plasma density depletion. The boundaries of the turbulent regions are abrupt, suggesting a threshold-driven or nonlinear onset.

The observed $\boldsymbol{B}$ and $\boldsymbol{E}$ indicate strong, intermittent turbulence. The PSD of $\boldsymbol{B}$ is consistent with a driving scale of $\sim 10^8$ m, an inertial range with wavenumbers up to $|\boldsymbol{k}|\rho_i = 1$ ($f \sim f_{\rm ci}$), and dissipation at larger wavenumbers and/or frequencies. The kurtosis in distributions of increments of $\boldsymbol{B}$ indicates non-Gaussian distributions at short time lags ($t_{\rm lag} < 1/f_{\rm ci}$) and relaxes to more Gaussian values at larger time lags, which is a sign of intermittency. When filtered to $f > f_{\rm ci}$, $\boldsymbol{E}$ has a defined correlation distance and time. The structures move at speeds that are consistent with the Alfvén speed, sound speed, or fast mode. It is difficult to distinguish between these notional speeds because they are nearly the same in this case. These observations suggest that $\boldsymbol{E}$ with $f > f_{\rm ci}$ consists of a set of pseudorandom small-scale structures rather than a mixture of linear wave modes. The PDF of $\boldsymbol{E}$ fits remarkably well to a stretched exponential ($e^{-\sqrt{|E|/E_0}}$).

The MMS encounter with a turbulent magnetic reconnection region affords a detailed view of the kinetic processes involved with charged particle heating and acceleration. Enhanced electron acceleration appears in short bursts of the order of a few seconds. Electron distributions have a characteristic shoulder at moderate energy (several times T_e; Figure 4(k)) that is most visible in a parallel slice (not shown). The thermal core of the electrons indicates that $T_{e\parallel} > T_{e\perp}$, whereas the higher-energy electrons often have higher perpendicular energy. In many events, accelerated electrons are in magnetic depletions and have perpendicular pitch angles, suggesting trapping. Almost all of the events have a large, positive perpendicular contribution of $\langle \boldsymbol{J}\cdot\boldsymbol{E}\rangle/\langle n\rangle$. The trapping and correlation with large, positive $\langle \boldsymbol{J}\cdot\boldsymbol{E}\rangle/\langle n\rangle$ indicate a local acceleration process.

The observed perpendicular pitch angles of high-energy electrons are in consort with observations of $\langle \boldsymbol{J}\cdot\boldsymbol{E}\rangle$, which show that the perpendicular contribution of $\langle \boldsymbol{J}\cdot\boldsymbol{E}\rangle$ greatly exceeds the parallel contribution (Figure 4(g)). The observation that $T_{e\parallel} > T_{e\perp}$ in the thermal core (Figure 4(l)), however, is puzzling. This enigma is explored in a companion paper (Ergun et al. 2020).

Ions appear to absorb the majority of the magnetic energy imparted into the particles inside of the turbulent region. The T_i outside of the turbulent region is roughly 4–5 keV. Inside of the turbulent region, T_i is roughly 20 keV with acceleration to 200 keV or greater. In the inertial region of turbulence, the energy at the driving range cascades to small scales (higher frequencies) where dissipation occurs. In most plasmas, this scale is at $|\boldsymbol{k}|\rho_i = 1$ ($f \sim f_{\rm ci}$), where ions can efficiently absorb energy, so strong ion heating is expected. The acceleration to higher energies appears to be enabled by trapping in magnetic depletions, which can greatly increase the dwell time of a particle in the heating regions.

5. Conclusions

The MMS satellites have made unique observations of local energization inside of a turbulent region driven by magnetic field annihilation, which, in turn, is enabled by magnetic reconnection. Strong turbulence appears to generate the necessary ingredients for the development of a significant nonthermal tail in both the electron and ion distributions. The turbulence cascades the driving energy to smaller scales and higher frequencies at which the charged particles can efficiently absorb energy. The observations suggest that enhanced ion heating via E_y in a reversing magnetic field (Speiser 1965), cyclotron-resonant acceleration of ions (e.g., Chang et al. 1986), second-order acceleration of electrons, double layers (e.g., Ergun et al. 2009), wave–particle interactions, Fermi acceleration (Drake et al. 2006), and magnetic pumping (betatron acceleration) are all active. Turbulence also generates magnetic depletions that trap the particles and impart unequal dwell times, causing relatively few particles to absorb a disproportionately large amount of energy.

The direct observation of nonthermal particle acceleration from strong turbulence has far-reaching implications. Turbulence is pervasive in plasmas and may occupy significant volumes of space. The volume occupied by the turbulent regions can be many orders of magnitude larger than the diffusion region of magnetic reconnection. Furthermore, turbulence has no limiting driving scale. For example, a supernova remnant (10^{17} m) may have a driving scale that is 9 orders of magnitude larger than the region that MMS observed (10^{8} m) and 10^{27} times the volume. It is possible, then, that turbulent acceleration may make a significant contribution to part of the cosmic-ray spectrum.

This work was funded by the NASA MMS project. The French LPP (SCM) involvement is funded by CNES and CNRS. The authors recognize the tremendous effort in developing and operating the MMS spacecraft and instruments and sincerely thank all involved. All of the data used in this paper are publicly available from the MMS Science Data Center.

ORCID iDs

R. E. Ergun https://orcid.org/0000-0002-3096-8579
J. E. Stawarz https://orcid.org/0000-0002-5702-5802
I. J. Cohen https://orcid.org/0000-0002-9163-6009
R. Nakamura https://orcid.org/0000-0002-2620-9211
J. L. Burch https://orcid.org/0000-0003-0452-8403

References

Alfvén, H. 1954, Tell, 6, 232
Andersson, L., Ergun, R. E., Tao, J., et al. 2009, PhRvL, 102, 225004
Angelopoulos, V., Baumjohann, W., Kennel, C. F., et al. 1992, JGR, 97, 4027
Angelopoulos, V., Kennel, C. F., Coroniti, F. V., et al. 1994, JGR, 99, 21257
Bandyopadhyay, R., Oughton, S., Wan, M., et al. 2018, PhRvX, 8, 041052
Baumjohann, W., Paschmann, G., & Cattell, C. A. 1989, JGR, 94, 6597
Birn, J., Drake, J., Shay, M., et al. 2001, JGR, 106, 3715
Blake, J. B., Mauk, B. H., Baker, D. N., et al. 2016, SSRv, 199, 309
Borovsky, J. E., Elphic, R. C., Funsten, H. O., & Thomsen, M. F. 1997, JPlPh, 57, 1
Burch, J. L., Moore, T. E., Torbert, R. B., & Giles, B. L. 2016, SSRv, 199, 5
Chang, T., Crew, G. B., Hershkowitz, N., et al. 1986, GeoRL, 13, 636
Cohen, I. J., Mitchell, D. G., Kistler, L. M., et al. 2017, JGRA, 122, 9282
Drake, J., Swisdak, M., Cattell, C., et al. 2003, Sci., 299, 873
Drake, J. F., Swisdak, M., Che, H., & Shay, M. A. 2006, Natur, 443, 553
Dungey, J. W. 1961, PhRvL, 6, 47
Dunlop, M. W., Balogh, A., Glassmeier, K.-H., & Robert, P. 2002, JGR, 107, 1384
Ergun, R. E., Ahmadi, N., Kromyda, L., et al. 2020, ApJ, 898, 153
Ergun, R. E., Andersson, L., Tao, J., et al. 2009, PhRvL, 102, 155002
Ergun, R. E., Goodrich, K. A., Stawarz, J. E., Andersson, L., & Angelopoulos, V. 2015, JGR, 120, 1832
Ergun, R. E., Goodrich, K. A., Wilder, F. D., et al. 2018, GeoRL, 45, 3338
Ergun, R. E., Tucker, S., Westfall, J., et al. 2016, SSRv, 199, 167
Goodrich, K. A., Ergun, R. E., & Stawarz, J. E. 2016, GeoRL, 43, 6044
Gosling, J. T. 2007, ApJ, 671, 73
Gosling, J. T., Skoug, R. M., McComas, D. J., & Smith, C. W. 2005, JGRA, 110, A01107
Hesse, M., Schindler, K., Birn, J., & Kuznetsova, M. 1999, PhPl, 6, 1781
Imada, S., Nakamura, R., Daly, P. W., et al. 2007, JGRA, 112, A03202
Koide, S., Kudoh, T., & Shibata, K. 2006, PhRvD, 74, 044005
Kumar, P., & Zhang, B. 2015, PhR, 561, 1
Le Contel, O., Leroy, P., Roux, A., et al. 2016, SSRv, 199, 257
Lichko, E., Egedal, J., Daughton, W., & Kasper, J. 2017, ApJL, 850, L28
Lindqvist, P.-A., Olsson, G., Torbert, R. B., et al. 2016, SSRv, 199, 137
Lu, S., Angelopoulos, V., Artemyev, A., et al. 2019, ApJ, 878, 109
Lyutikov, M., Pariev, V. I., & Blandford, R. D. 2003, ApJ, 597, 998
Mauk, B. H., Blake, J. B., Baker, D. N., et al. 2016, SSRv, 199, 471
Nagai, T., Fujimoto, M., Saito, Y., et al. 1998, JGR, 103, 4419
Øieroset, M., Lin, R. P., Phan, T. D., Larson, D. E., & Bale, S. D. 2002, PhRvL, 89, 195001
Øieroset, M., Phan, T. D., Fujimoto, M., Lin, R. P., & Lepping, R. P. 2001, Natur, 412, 414
Parker, E. N. 1957, JGR, 62, 509
Paschmann, G. 2008, GeoRL, 35, L19109
Paschmann, G., Papamastorakis, I., Sckopke, N., et al. 1979, Natur, 282, 243
Pollock, C., Moore, T., Jacques, A., et al. 2016, SSRv, 199, 331
Priest, E. R., & Forbes, T. G. 2002, A&ARv, 10, 313
Retinó, A., Nakamura, R., Vaivads, A., et al. 2008, JGR, 113, A12215
Russell, C. T., Anderson, B. J., Baumjohann, W., et al. 2016, SSRv, 199, 189
Speiser, T. W. 1965, JGR, 70, 4219
Spruit, H. C., Daigne, F., & Drenkhahn, G. 2001, A&A, 369, 694
Stawarz, J. E., Ergun, R. E., & Goodrich, K. A. 2015, JGRA, 120, 1845
Stawarz, J. E., Eriksson, S., Wilder, F. D., et al. 2016, JGR, 121, 11021
Taylor, G. I. 1938, RSPSA, 164, 476
Thompson, C. 1994, MNRAS, 270, 480
Torbert, R. B., Burch, J. L., Phan, T. D., et al. 2018, Sci., 362, 1391
Torbert, R. B., Russell, C. T., Magnes, W., et al. 2016, SSRv, 199, 105
Uzdensky, D. A., Cerutti, B., & Begelman, M. C. 2011, ApJL, 737, L40
Vaivads, A., Retino, A., Khotyaintsev, Y. V., & Andre, M. 2011, AnGeo, 29, 1917
von Goeler, S., Stodiek, W., & Sauthoff, N. 1974, PhRvL, 33, 1201
Vörös, Z., Baumjohann, W., Nakamura, R., et al. 2004, JGRA, 109, A11215
Weygand, J. M., Kivelson, M. G., & Khurana, K. K. 2005, JGR, 110, 1205
Yamada, M., Kulsrud, R., & Ji, H. 2010, RvMP, 82, 603
Zank, G. P., Hunana, P., Mostafavi, P., et al. 2015, ApJ, 814, 137
Zank, G. P., le Roux, J. A., Webb, G. M., Dosch, A., & Khabarova, O. 2014, ApJ, 797, 28
Zhao, L.-L., Zank, G. P., Chen, Y., et al. 2019, ApJ, 872, 4
Zhao, L. L., Zank, G. P., Khabarova, O., et al. 2018, ApJL, 864, L34
Zweibel, E. G. 1989, ApJ, 340, 550